A High Dynamic Range Closed-Loop Stiffness-Adjustable MEMS Force Sensor

Mohammad Maroufi [iD], Hamed Alemansour [iD], and S. O. Reza Moheimani [iD], *Fellow, IEEE*

Abstract—We present a microelectromechanical system (MEMS)-based closed-loop force sensor, capable of measuring bidirectional forces along one axis of motion. The device comprises an on-chip electrothermal displacement sensor and electrostatic actuators. It features a voltage-controlled stiffness-adjustment mechanism, providing the user with an additional means of tuning the sensor's characteristics. This silicon-on-insulator device is an improvement on our previous design, offering a better dynamic range and a less complex calibration process. The sensor is fabricated based on a standard SOI MEMS process. It is then fully characterized and instrumented with a feedback controller. The closed-loop characterization reveals a 1σ-resolution of 4.74 nN and a force sensing range of $-211.7\,\mu$N to $211.5\,\mu$N, leading to a dynamic range of 92.9 dB. [2019-0248]

Index Terms—Force sensor, microelectromechanical systems (MEMS), electrothermal sensor, electrostatic actuator, stiffness adjustment mechanism.

I. INTRODUCTION

THE ability to measure force on micro- and nano-sized samples is of significance in many fields of science and technology. Numerous applications in material science, surface chemistry, biochemistry and biology can greatly benefit from such measurements. Miniaturized force sensors have paved the way for high-precision force measurements from pico- to nano-newtons in a variety of applications [1]–[6].

Although the atomic force microscope (AFM) is primarily used for imaging, its cantilever can be used as a force sensor by obtaining the force-distance curve [7], [8]. Measuring adhesive interaction forces in hydrogen bonds [9], determining mechanical properties of proteins [2], [3], and obtaining cell and bacteria rigidity [10]–[12] are examples of successful AFM force spectroscopy.

A viable technology for force sensor fabrication is based on microelectromechanical systems (MEMS) technology [13], [14]. Contrary to the AFM, a variety of mechanisms can

be implemented in MEMS, enabling the tuning of wide-range force sensor parameters. MEMS force sensors have been used in a variety of applications. In [1], a MEMS force sensor is proposed for measuring the stiffness of hydrogel microparticles. AFM microcantilevers are characterized by a MEMS force sensor in [4], and [5]. In [15], and [16] a MEMS force sensor is designed and implemented to measure flight forces in a fruit fly. The force-deformation response of axons in fruit flies has also been investigated by proposing another large-range MEMS force sensor in [6].

MEMS-based static force sensing can be performed in either open or closed loop. In the former approach, variation in one of the sensor's parameters due to the external force, typically a mechanical displacement/deformation, is measured and then interpreted as force. In the closed-loop approach, the sensor features an actuation mechanism to counterbalance the input force, and therefore, the actuation signal becomes a measure of the input force. This approach eliminates the nonlinearities originating from flexural mechanisms. Consequently, the sensor will have a larger measurement range, leading to a wider dynamic range.

Authors of [17], report a closed-loop MEMS force sensor equipped with comb-drive electrostatic actuators. However, their device lacks an embedded displacement measurement mechanism. Comb-drive actuators and capacitive sensors are used in a MEMS force sensor reported in [18], where a measurement range of $60\,\mu$N is reported with a resolution of $2.8\,$nN. In [19], a MEMS force sensor is designed and fabricated, also benefiting from electrostatic actuation and integrated capacitive sensor. This sensor is used in closed loop to measure the surface tension of various liquids.

We reported a closed-loop force sensor in [20], [21] and demonstrated its functionality by measuring the stiffness of AFM microcantilevers. The sensor achieved a dynamic range of $71.2\,$dB, and was capable of measuring linear forces in both push and pull orientations. In addition, the sensor featured an embedded stiffness-adjustment mechanism to enable tuning of the device's stiffness *in situ*.

The device reported in [20], however, requires a relatively complicated calibration procedure and has a limited force measurement range. The modified closed-loop force sensor reported here, addresses these issues. In particular, we have been able to increase the measurement range of the sensor by a factor of five, while maintaining the device stiffness at the same level as [20]. Furthermore, the new design features a displacement amplification mechanism to enhance resolution of the embedded electrothermal displacement sensor,
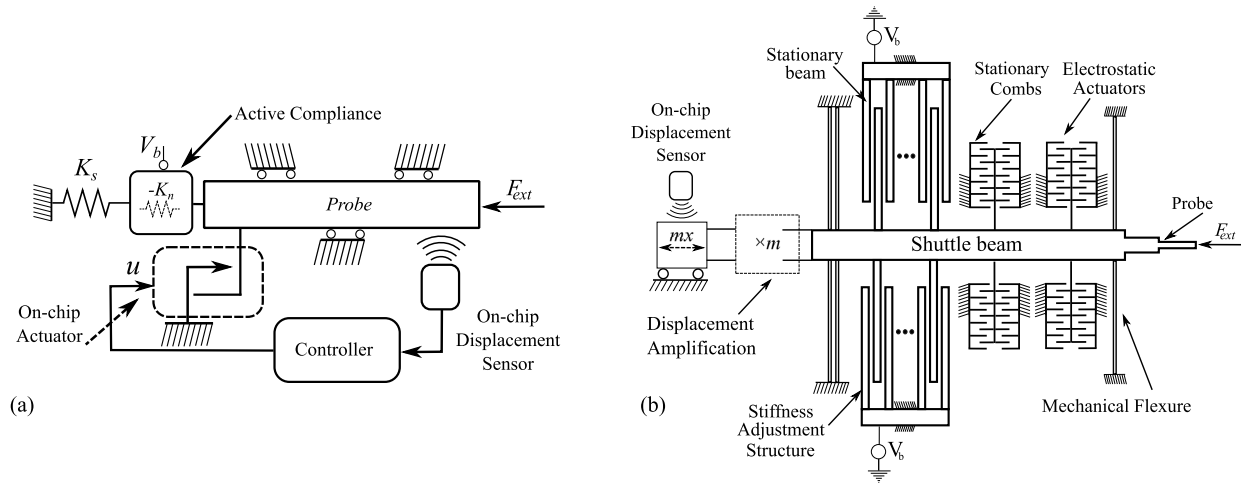
Fig. 1. (a) Principle of operation of the closed-loop force sensor. The device includes a stiffness adjustment mechanism that adds a negative stiffness tuned by V_b. The total stiffness then is equal to $(K_s - K_n)$. (b) Schematic of the proposed force sensor. The displacement amplifier mechanically amplifies the displacement of the shuttle beam by a factor of m before being measured by the embedded displacement sensor.

providing a sub-nanometer 1σ-resolution. Moreover, a more straightforward calibration procedure is proposed here that employs two sets of push-pull electrostatic actuators.

The remainder of the paper continues as follows. In Sec. II, the force sensor design is detailed. The fabrication of the force sensor is explored in Sec. III. Sec. IV details the force sensor characterization and calibration. The design and implementation of a controller is discussed in Sec. V. In Sec. VI, the application of the force sensor in measuring the stiffness of AFM cantilevers is presented. Discussion and comparison with previous works are reported in Sec. VII and the paper is concluded in Sec. VIII.

II. FORCE SENSOR DESIGN

The force sensor is designed to be operated in closed loop. The working principle of the device is schematically shown in Fig. 1a. The external force (F_{ext}) induces an initial displacement on the shuttle beam. The displacement is then measured using an embedded displacement sensor. The feedback controller, designed to track a zero-displacement set point, generates a command signal (u) that causes the embedded actuators to produce a counter-balance force, pushing back the shuttle beam to its null position. In steady state, the control signal u is proportional to the external force, and can be expressed in μN provided that the device is fully characterized. The sensor resolution is a function of the noise content of u. Note that since the displacement of the shuttle beam remains within the resolution of the embedded displacement sensing mechanism, the device will function as a linear system.

Mechanical stiffness of the force sensor has an immediate effect on its sensitivity. Additionally, the relative stiffness of the force sensor and sample can play a crucial role in the accuracy of measurements obtained from delicate samples. These are the main reasons for incorporating a stiffness adjustment mechanism in our design [20]. As shown in Fig. 1a, the active compliance mechanism adds a negative stiffness of $-K_n$ to the mechanical flexures. This stiffness is controlled by the applied voltage V_b. A detailed discussion on the

open- and close-loop measurements and the ramifications of having a large stiffness mismatch between the force sensor and the sample can be found in [20].

Fig. 1b illustrates a more detailed view of the force sensor design. The device comprises a shuttle beam at the center interacting with the sample through a probe at one end. Two sets of electrostatic actuators are implemented, making the closed loop operation of the force sensor possible. Clamped-guided beams are used as mechanical flexures. The displacement range of the shuttle beam is increased using an amplification mechanism to enhance the displacement measurement resolution of the device. An electrothermal displacement sensor is embedded within the device to measure the amplified displacement of the shuttle beam. A stiffness-adjustment mechanism enables control of the device's stiffness. The design of each part is further detailed next.

A. Electrothermal Displacement Sensor

In [20], we employed a bulk piezoresistive displacement sensor, which contains two pairs of slightly tilted beams in a V-shaped configuration. This piezoresistive sensor has a nanometer range resolution over a relatively large bandwidth [22], [23]. These tilted beams also function as a mechanical flexural mechanism, adding a relatively large extra mechanical stiffness to the sensor. This phenomenon is more significant here since the device thickness is increased from $10\,\mu$m to $25\,\mu$m to achieve a larger actuation force and out-of-plane rigidity.

To address this issue, we incorporated a non-contact electrothermal displacement sensor to measure shuttle beam's displacement. This sensor has a simple structure, can be fabricated using a single mask, and requires a straightforward circuitry for readout [24]–[26].

As schematically shown in Fig. 2a, the electrothermal sensor comprises two micro-heaters placed on the same plane as the heat sink. As the heat sink displaces in parallel with the heaters, the overlapped area between the micro-heaters and the heat sink varies, changing the rate of heat transfer between
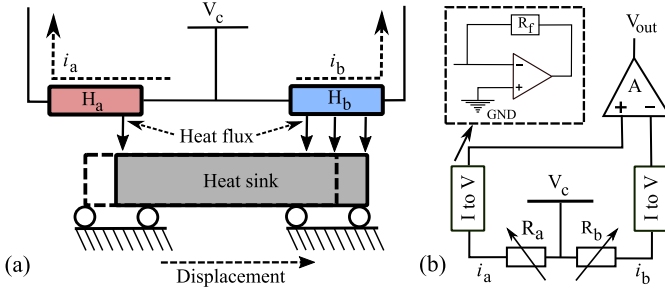
Fig. 2. (a) Working principle of electrothermal sensor for measuring rectilinear displacement of the heat sink. Here, H_a and H_b are the silicon heaters. (b) The trans-impedance readout circuit.

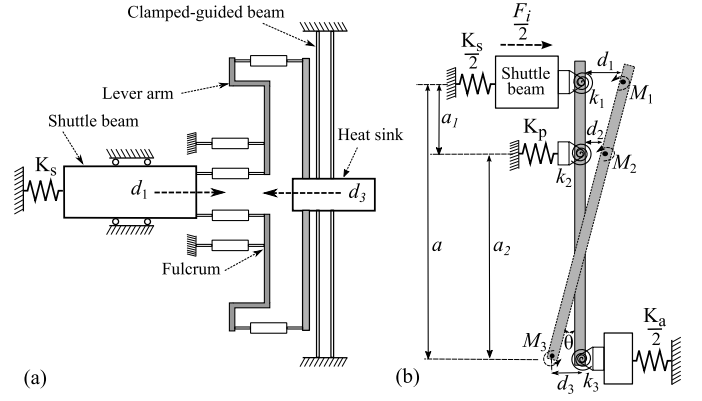

Fig. 3. (a) The displacement amplification structure comprising a pair of leverage mechanisms. (b) The free-body-diagram model of one lever arm.

the two. Heat transfer fluctuations lead to an opposite change in the temperature and consequently the resistance of the heaters. As shown in Fig. 2b, this opposite resistance change is converted to voltages using trans-impedance amplifiers and then is differentially amplified at the output. The gain of one of trans-impedance amplifiers is adjustable to remove the bias at the electrothermal sensor output at null position.

Electrothermal displacement sensors, however, have an inferior resolution compared with bulk piezoresistive sensors [27]. To enhance their measurement resolution, we designed the device so that the displacement of the shuttle structure is measured by the sensor after it is mechanically amplified.

B. Displacement Amplification Mechanism

The amplification mechanism is shown in Fig. 3a. Here, the shuttle beam and the heat sink displacements are denoted by d_1 and d_3, respectively. Thus, the amplification ratio is defined as

$$m = \left| \frac{d_3}{d_1} \right|. \tag{1}$$

In order to realize the fulcrum of the lever mechanism, a compact compliance structure such as a flexural joint may be used. These joints can be designed in different geometries such as circular, elliptical, and corner filleted [28]. However, they can add a large rotational stiffness to the design, which could be difficult to reduce due to the minimum feature size allowed by the micro-fabrication process.

Another method of realizing the joints is to use distributed compliance flexures, such as beams. In this work, we use three-sectioned beams that function as fulcrum and as joints connecting lever arms to the shuttle beam and the heat sink. Additionally, since the lever mechanisms generate a curve-shaped loci, a guide mechanism is also implemented for the heat sink to achieve a rectilinear motion. To do so, four clamped-guided beams are employed as shown in Fig. 3a.

In order to analytically investigate the amplification ratio as well as the stiffness with the amplification mechanism, the free body diagram of the system is shown in Fig. 3b. Here, the rotational and longitudinal stiffnesses of the three-sectioned beams are modeled as rotational and linear springs, respectively. The goal is to obtain the displacement d_i ($i = 1$ to 3) in the presence of an input force (F_i). The total stiffness of the clamped-guided beams on the heat sink side is designated

by K_a, and K_s denotes the total stiffness of the flexures connected to the shuttle. Due to symmetry, half of these stiffnesses and the input force (i.e. $F_i/2$) are considered for one arm. Assuming force equilibrium conditions, we have:

$$\frac{F_i}{2} = \frac{K_s}{2}d_1 + K_p d_2 - \frac{K_a}{2}d_3. \tag{2}$$

Considering the arm rigidity, we may write:

$$\frac{d_1 - d_2}{a_1} = \frac{d_3 + d_2}{a_2}. \tag{3}$$

To obtain the next equation, we note that the arm undergoes a rotation of θ radians. Having the rotational stiffnesses of the three sectioned beams (see Appendix), we can write the condition for rotational equilibrium around the fulcrum as:

$$\frac{F_i}{2}a_1 = k_1\theta + k_2\theta + k_3\theta + \frac{K_s}{2}d_1 a_1 + \frac{K_a}{2}d_3 a_2 \tag{4}$$

where

$$\theta = \frac{d_1 - d_2}{a_1}. \tag{5}$$

Solving (2), (3), and (4), simultaneously, d_i ($i = 1$ to 3) can be obtained in presence of an input force (F_i). Knowing the displacements, we obtain the total stiffness of the force sensor with the amplification mechanism as:

$$K_t = \frac{F_i}{d_1} \tag{6}$$

The 1σ-resolution of an electrothermal sensor is typically in the range of 2 nm to 3 nm [29], depending on the measurement bandwidth. In order to achieve a better resolution compared to bulk piezoresistive sensors reported in [20], we design the device with an amplification ratio of $m = 2.5$.

Note that the design of the amplification mechanism is based on the assumption that displacement movements remain small when the device is operational. Since the force sensor is used in closed loop, this is a valid assumption.

C. Mechanical Flexures

The flexural mechanism is realized using clamped-guided beams. The transverse stiffness (K_c) of each beam, assuming
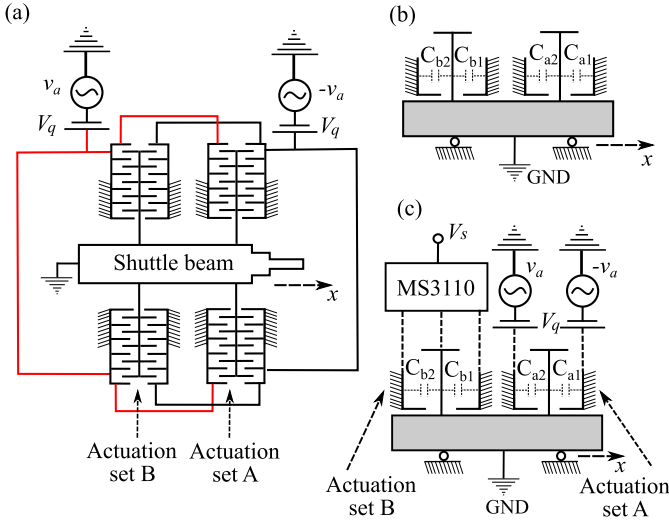
Fig. 4.   (a) Electrostatic actuators are used in the force sensor. (b) The total capacitance of each side of the electrostatic actuators. (c) The test setup implemented to experimentally identify actuator parameters.

small displacements, can be obtained from

$$K_c = \frac{Ew^3t}{l^3}. \tag{7}$$

Here, l is the beam's length, E is the Young's modulus of silicon, t is the device thickness, and w is the width (in-plane dimension) of the beam.

The initial displacement of the shuttle beam upon exertion of the external force is inversely proportional to the flexural mechanism's transverse stiffness. Resolution of the embedded displacement sensor is limited, and thus, minimizing this stiffness can enhance the force sensor sensitivity. This is valid both for open- and closed-loop force sensing modalities.

The resonant frequency of the device is another factor influenced by transverse stiffness. By constructing a finite element model (FEM) in CoventorWare software, we were able to tune dimensions of the beams so that the fundamental resonant mode of the system occurs along the transverse motion of the shuttle beam. This reduces the complexity of designing a controller for the force sensor.

The longitudinal stiffness of clamped-guided beams plays a crucial role in preventing electrostatic actuators from experiencing snap-in instability [30], [31]. For small displacements, this stiffness is obtained as follows:

$$K_l = \frac{Ewt}{l}. \tag{8}$$

The beams dimensional tuning is performed to achieve a high enough longitudinal stiffness in order to prevent the electrostatic actuators from experiencing snap-in instability. This orders of magnitude higher stiffness also renders the sensor immune to transverse in-plane parasitic forces.

D. Electrostatic Actuators

The electrostatic actuators, shown in Fig. 4a, consist of two sets of comb-drives. Magnitude of the attractive

force in a comb-drive with an actuation voltage of V is expressed as [30]:

$$F_{act} = \frac{1}{2} \left| \frac{\partial C}{\partial x} \right| V^2. \tag{9}$$

As shown in Fig. 4a, differential actuation voltages (i.e. $\pm v_a$) are added to a bias voltage (V_q) and applied to the stationary combs, while the moving combs are electrically grounded. This arrangement allows for bidirectional force measurement. To obtain the resulting force, we define actuation coefficients based on the rate of change of comb capacitances

$$k_{a1,2} = \frac{\partial C_{a1,2}}{\partial x} \quad \& \quad k_{b1,2} = \frac{\partial C_{b1,2}}{\partial x} \tag{10}$$

From (9), we determine the force exerted on the shuttle beam by actuator set A as

$$F_A = \frac{(k_{a2} - k_{a1})}{2} \left[v_a^2 + V_q^2 \right] + (k_{a2} + k_{a1}) V_q v_a. \tag{11}$$

Similarly, for actuation set B, the force is

$$F_B = \frac{(k_{b2} - k_{b1})}{2} \left[v_a^2 + V_q^2 \right] + (k_{b2} + k_{b1}) V_q v_a. \tag{12}$$

The total force exerted on the shuttle beam is then:

$$F_n = F_A + F_B \tag{13}$$

That is:

$$F_n = \left[\frac{k_{a2} + k_{b2} - k_{a1} - k_{b1}}{2} \right] \left(v_a^2 + V_q^2 \right) + \left(\sum_{i=1}^{2} k_{ai} + \sum_{i=1}^{2} k_{bi} \right) V_q v_a \tag{14}$$

To determine the relationship between v_a and the resulting force, we propose a novel calibration procedure to experimentally identify the parameters in (14). This is explained in Sec. IV-C.

E. Stiffness Adjustment Mechanism

In a manner similar to [20], we design a trapezoidal-shaped parallel plate capacitive structure to function as a stiffness adjustment mechanism. The trapezoidal shape of the electrodes reduces the added mass of this structure [32]. We apply a bias voltage of V_b to the stationary electrodes, while the moving electrodes are electrically grounded through the shuttle structure. At the null position, each moving electrode is positioned half way between the two stationary electrodes. Hence, the attractive electrostatic forces cancel each other out. However, the attractive force on each side rapidly changes as the moving electrodes displace in one direction, causing a net force that pushes the electrodes further away from their equilibrium (null) position. In absence of a restoring force, the displacement increases rapidly, causing the moving and stationary electrodes to ultimately snap in.

We showed in [20] that the net force on moving electrodes is a function of their displacement from the null position. Therefore, considering the direction of the force, we can define a negative stiffness as $K_n = -\frac{\partial F_{net}}{\partial x}$, whose magnitude
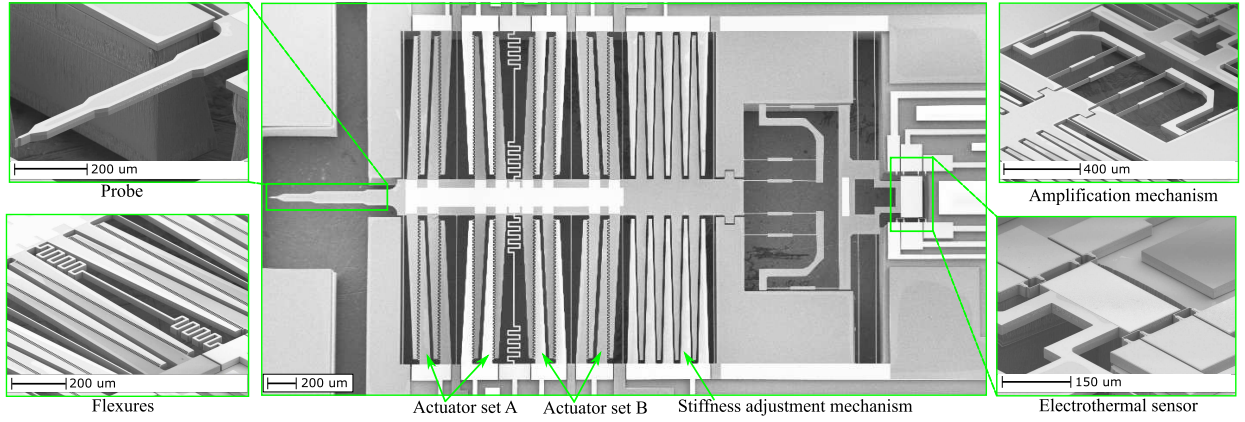
Fig. 5. SEM micrograph of the force sensor. Close up views show the force sensor tip, the amplification mechanism for the embedded displacement sensor, the electrothermal displacement sensor, and the electrostatic actuators.

is adjustable by applying the electrical bias voltage (V_b). Assuming the initial gap between the electrodes is d_0 and their overlapped length is L, the negative stiffness for n moving electrodes is [20]:

$$K_n = -\frac{4n\epsilon_0 Lt}{d_0^3}\cos^2(\theta)\,V_b. \qquad (15)$$

Here, t is the (out of plane) thickness of the electrodes, ϵ_0 is the air permittivity, and θ is the inclination angle of the trapezoid sides. Note that the negative stiffness in (15) is obtained for a small displacement relative to the electrodes initial gap (i.e. $x \ll d_0$) [20]. This condition is justified since the force sensor functions in closed-loop.

III. FORCE SENSOR FABRICATION

The force sensor was fabricated using the MEMSCap's silicon-on-insulator (SOI) microfabrication process, SOIMUMPs. The process starts with a SOI wafer with $25\,\mu$m thick device layer. To increase electrical conductivity, doping at the top surface of the device layer is enhanced using thermal diffusion. Then, using thermal deposition, a layer of gold and chromium is deposited and patterned for electrical routing. Using deep reactive ion etching the device layer is patterned afterwards. Finally, the substrate and the buried oxide layers are etched using a wet and dry etch and the device is released.

A scanning electron microscope (SEM) micrograph of the fabricated device is shown in Fig. 5. The shuttle beam with dimensions of $2.382\,\text{mm} \times 0.250\,\text{mm}$ and the multi-sectioned probe at its extremity are visible. Dimensions of the force sensor are presented in Table I. The relatively large length of the probe makes it suitable for interacting with various types of samples. The probe's width is gradually reduced to maintain its out-of-plane rigidity, reaching $2\,\mu$m at the tip.

IV. CHARACTERIZATION

After the force sensor fabrication, the cap around the probe is manually broken using a diamond knife to expose the tip. The device is then wire-bonded on a custom-designed printed circuit board (PCB). The readout circuit for the electrothermal

TABLE I
THE GEOMETRICAL PROPERTIES OF THE FORCE SENSOR

Stiffness	Overlap $L \simeq 985\,\mu$m		Air gap $d_0 = 13\,\mu$m
Adj. Structure	Trapezoidal: Length: 1.01 mm, Bases: $74\,\mu$m, $24\,\mu$m		
Electrostatic	Air gap $g = 2\,\mu$m		Engagement:$4\,\mu$m
Actuators	Trapezoidal: Length: 1 mm, Bases: $75\,\mu$m, $25\,\mu$m		
Clamped-guided	Length $1035\,\mu$m		Width $7\,\mu$m, No. 2
Flexures	Length $1035\,\mu$m		Width $5.5\,\mu$m, No. 8
Probe	Length: $800\,\mu$m, Width: $2\,\mu$m to $110\,\mu$m		

sensor (shown in Fig. 2b) is separately implemented on a signal conditioning PCB. For actuation, the circuit in Fig. 4a is externally implemented using commercial amplifiers and DC sources. Both sets are actuated using the same source, while V_q is set to $25\,\text{V}$.

A. In-Plane Static Response

A laser-Doppler vibrometer, Polytec Micro System Analyzer (MSA-100-3D), is used to measure the in-plane rectilinear displacement of the shuttle beam. The displacement is shown in Fig. 6a as a function of actuation voltage for different stiffness adjustment voltages ranging from $0\,\text{V}$ to $60\,\text{V}$. The overall stiffness of the device decreases at higher stiffness adjustment voltages, as observed by increasing displacement range in inset of Fig. 6a.

Output of the electrothermal sensor is recorded and plotted against shuttle beam displacement for all stiffness adjustment voltages in Fig. 6b. We observe the same linear trend at all voltages, and the averaged calibration factor[1] for the embedded electrothermal sensor is obtained as $1.672\,\mu m/V$.

To determine the resolution of the electrothermal sensor, its output is recorded for $20\,\text{s}$ using a dSPACE MicroLab-Box with the sampling rate of $25\,\text{kHz}$. A low-pass (SR650 Stanford Research Systems) with corner frequency of $2\,\text{kHz}$ and a roll off of $115\,\text{dB/octave}$ is placed on the path to limit the bandwidth and eliminate aliasing. The tests are

---

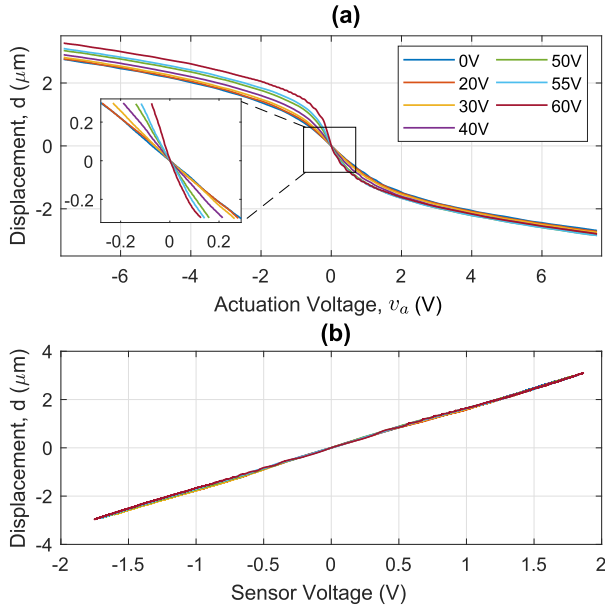[1]The calibration factor is defined as the slope of the curve in Fig. 6b.

Fig. 6.   (a) Probe's displacement versus the actuation voltage (v_a) for stiffness adjustment voltages ranging from 0 V to 60 V. (b) The shuttle beam displacement as a function of the electrothermal sensor voltage output for the same range of stiffness-adjustment voltages.

performed on an optical table to minimize external disturbances. The output voltage is converted to displacement and a 1σ-resolution of 0.645 nm is obtained for the electrothermal sensor. This sub-nanometer resolution compared to the prior art in [29] shows that the amplification mechanism can effectively enhance the precision of the electrothermal sensor. Note that resolution of the electrothermal sensor remains invariant for all stiffness adjustment voltages as expected.

B. Frequency Response Measurement

Frequency response of device from the electrostatic actuation input to electrothermal sensor output is obtained over a frequency range of 4 kHz using a CF-9400 ONO SOKKI FFT analyzer. The results are shown in Fig. 7 for various V_b voltages. By increasing the stiffness adjustment voltage form 0 V to 60 V, the resonant frequency is reduced from 978 Hz to 568 Hz and the DC gain is raised by 9.5 dB. This can be interpreted as a threefold decrease in the stiffness and indicates the possibility of tuning the device's stiffness using the stiffness adjustment mechanism.

C. Calibration and Parameter Identification

In order to calibrate the sensor, we need to determine the force generated by the actuators as a function of the command voltage (u in Fig. 1a). Eq. (14) relates the actuation voltage (v_a) to the resulting force and contains four unknown actuation coefficients (i.e. $k_{a1,2}$ and $k_{b1,2}$). We employ an empirical approach to obtain these unknown parameters as well as the mechanical stiffness of the force sensor (K_t).

During the test, the comb drives on either side of each actuation set are separately actuated by a voltage (V). From (9), the force that is generated by each comb drive can be calculated.
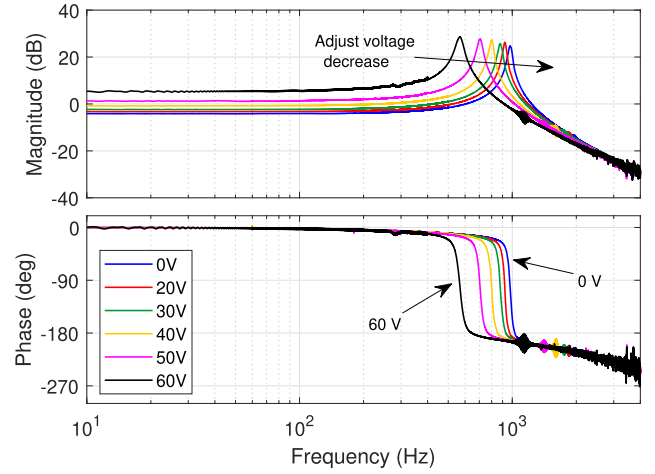

Fig. 7.   Frequency response of the force sensor from the actuation voltage input to the electrothermal sensor output for different V_b values.

Knowing the actuation force exerted on the shuttle beam, we can determine the displacement (x) from Hook's law as

$$x = QV^2 \tag{16}$$

where Q is defined in (17) for actuation set A.

$$Q_{ai} = \frac{k_{ai}}{2K_t}, \quad i = 1, 2 \tag{17}$$

Similarly, for the actuation set B we have:

$$Q_{bi} = \frac{k_{bi}}{2K_t}, \quad i = 1, 2. \tag{18}$$

During these four experiments, the comb drives are actuated one by one and the shuttle beam displacement is recorded with the MSA. The actuation voltage is adjusted to a displacement range of $\pm 0.5\,\mu$m, minimizing the flexural nonlinearities which may arise at large deflections. From (16) and the experimental data, $Q_{a1,2}$ and $Q_{b1,2}$ are determined.

In order to determine the five unknowns (i.e. $k_{a1,2}$, $k_{b1,2}$ and K_t), we perform an experiment which is schematically shown in Fig. 4c. Here, the actuation set A is being actuated while the differential change in the capacitance of the actuation set B is measured with a MS3110 evaluation board. The output voltage of MS3110 is proportional to the capacitance change experienced by the actuation set B (i.e. $V_s \propto |C_{b2} - C_{b1}|$). During the experiment, displacement of the shuttle beam is directly measured with the MSA while the displacement range is maintained at about $\pm 0.6\,\mu$m to minimize nonlinearities. Knowing the displacement range (Δx) and the output of the MS3110 (V_s), we can write:

$$k_{b1} + k_{b2} = \frac{C_M V_s}{\Delta x} \tag{19}$$

where C_M is the MS3110 calibration factor, i.e. 0.450 pF/V. Solving (16) and (19) simultaneously, the coefficients for both actuation sets as well as the force sensor stiffness are obtained and reported in Table II.

After the actuation coefficients are determined, the total force in Newtons generated by all actuators is obtained

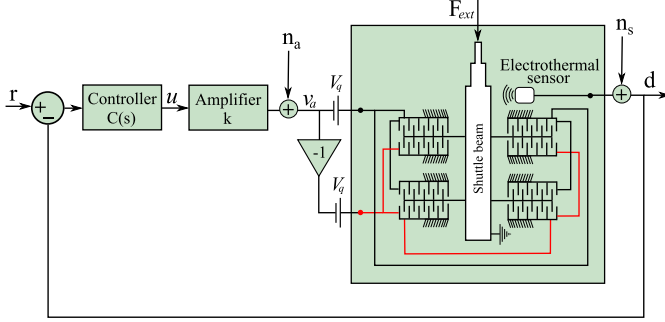| K_t	k_{a1}	k_{a2}	k_{b1}	k_{b2}
25.4	9.57	9.10	9.02	9.12

Fig. 8. Force sensor control system. F_{ext} shows the external force applied to the shuttle beam. The controller commands the electrostatic actuators to produce the same amount of force in the opposite direction to keep the shuttle beam's displacement zero.

Fig. 9. The frequency response of identified model along with the experimentally obtained response for the stiffness-adjustment voltage of 0 V.

from (13) as follows:

$$F = -1.9026 \times 10^{-10}v_a^2 + 9.2033$$
$$\times 10^{-6}v_a - 1.1892 \times 10^{-6}. \quad (20)$$

There is an offset force in (20) when the actuation voltage v_a is zero and only V_q is being applied. This term appears due to the slight asymmetric structure of the electrostatic actuators originated from microfabrication tolerances. This small force (about 1.2 μN) induces a small deflection (47.2 nm) within the sensor before an external force is applied. This is measured by the displacement sensor, and is then removed using the controller logic implemented in dSPACE. Therefore, the feedback loop is closed on a zero biased system, and the command signal (u in Fig. 1a) can be converted to force by the following equation during closed-loop force measurements:

$$F = -1.9026 \times 10^{-10}v_a^2 + 9.2033 \times 10^{-6}v_a \quad (21)$$

V. CONTROLLER DESIGN AND IMPLEMENTATION

The system dynamics can be identified from the frequency response plotted in Fig. 7. We only present the results for zero stiffness adjustment voltage; however, the same procedure can be applied otherwise. A third-order model is fitted to the frequency domain data, using the least-squares method. The identified transfer function, with the DC gain adjusted to unity, can then be expressed as:

$$G(s) = \frac{-2.01 \times 10^{-5}s + 0.9825}{8.53 \times 10^{-13}s^3 + 2.67 \times 10^{-8}s^2 + 3.78 \times 10^{-5}s + 1} \quad (22)$$

As shown in Fig. 9, the frequency domain response of the identified transfer function perfectly matches the experimentally obtained response.
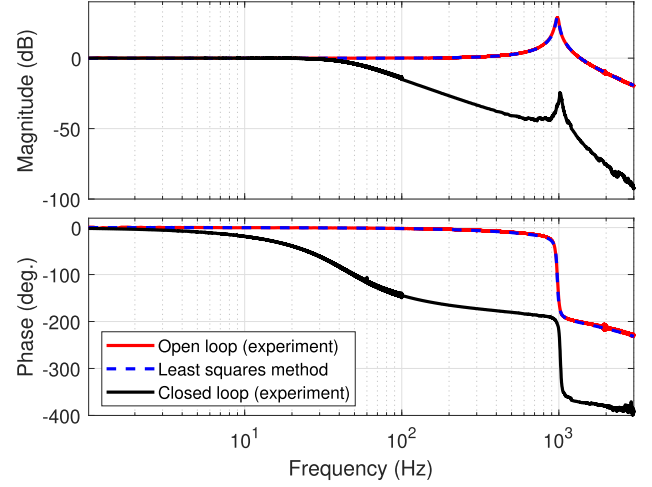
A feedback control system is designed to nullify the effect of external force on the force sensor's displacement. The closed-loop system does not require a high tracking bandwidth since it is meant to be used for measuring quasi-static loads. The system, however, does require good stability margins since its dynamics may alter as soon as it touches an external object. The feedback control system is shown in Fig. 8. The controller, C(s), is realized by cascading an integrator with a lag compensator in order to provide both a large stability margin and a good low-frequency tracking performance. Due to this large stability margin, the controller can work with different stiffness adjustment voltages without any modification. The controller is finely tuned using MATLAB control system designer toolbox and is obtained as:

$$C(s) = \frac{3.5(s + 24000)}{s(s + 380)}. \quad (23)$$

In Fig. 9, the closed-loop frequency response of the force sensor is compared to the open loop response. The tracking bandwidth is 44 Hz and remains nearly the same for other stiffness adjustment voltages. The gain and phase margins for $V_b = 0 V$ are 41.1 dB and 62 degrees, respectively, changing to 32.3 dB and 64 degrees for $V_b = 60 V$.

VI. FORCE SENSING PERFORMANCE

A. Force Sensing Resolution

We can obtain the force sensor resolution by determining noise content of the actuation signal (v_a in Fig. 8). This noise N is a function of the electrothermal sensor noise n_s and the actuation signal noise n_a as stated below.

$$N = \frac{-kC(s)}{1 + kC(s)G(s)}n_s(s) + \frac{1}{1 + kC(s)G(s)}n_a(s) \quad (24)$$

This noise is clearly a function of the sensor's dynamics (i.e. $G(s)$), and hence resolution of the force sensor would change with the stiffness adjustment voltage.

We recorded the noise at the sampling rate of 100 kHz using a dSPACE MicroLabBox. A low-pass filter (SR650
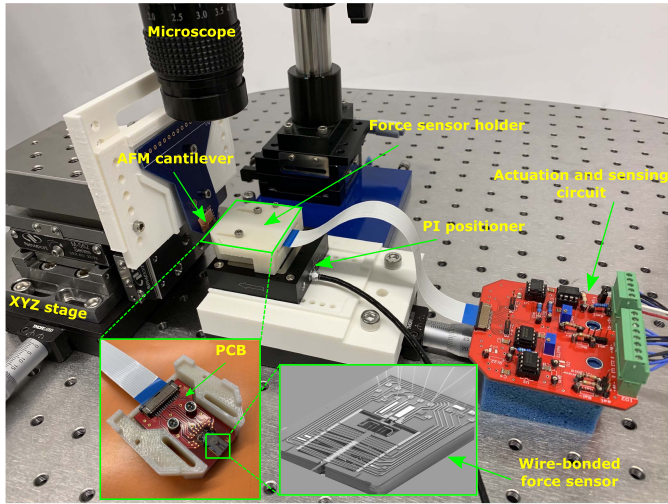
Fig. 10. The constructed experimental test setup for measuring the stiffness of AFM cantilevers.

TABLE III
SPECIFICATIONS OF CANTILEVERS USED IN EXPERIMENTS AND THEIR MEASURED STIFFNESSES

Cantilever	Model	Stiffness (N/m)			
		Min.	Max.	Nom.	Measured
Bruker	RTESP-525	100	400	200	187.65
AppNano	SHOCON	0.01	0.60	0.14	0.52

Stanford Research Systems) with the bandwidth 700 Hz and 115 db/Octave roll off was also used on the path to limit the bandwidth. The controller in (23) is implemented by an analog circuit. The noise signal is recorded over a 20 s time period, which is then converted to force using (21). For the stiffness adjustment voltages of 0 V, 40 V, and 60 V, the 1σ-resolutions of 4.74 nN, 4.66 nN and 4.38 nN are respectively obtained.

B. Stiffness Measurement Test

The force sensor is used to measure the stiffness of two different AFM cantilevers. The test setup is shown in Fig. 10. The cantilevers are glued to a PCB, which is then screwed through a custom-made adapter to a XYZ positioning stage (Newport M-562-XYZ ULTRAlign). The force sensor's PCB is also placed in a custom-made 3D printed casing and then immobilized on a PI P-622.1CD Piezo Linear Precision positioner. The PI positioner is connected to a Thorlabs PT1/M uni-axial stage for coarse positioning of the force sensor.

The cantilevers spring constants are in the range summarized in Table III. We operate the force sensor in closed loop to determine the cantilever stiffness with high precision. We bring the tip of the cantilever and the force sensor close to each other using the manual positioners. Then we use the PI positioner to move the force sensor closer to the cantilever tip, while monitoring the force. The approach process is stopped after the initial contact is established. Then, the positioner is commanded to move forward, pushing the force sensor to deflect the cantilever.
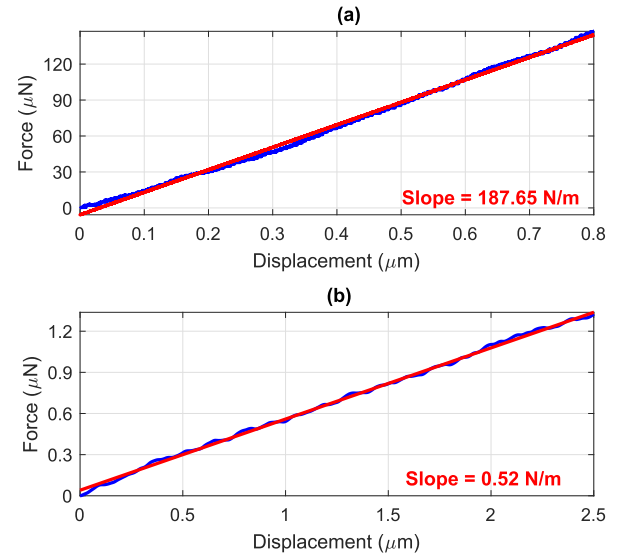

Fig. 11. The measured force as a function of tip deflection for (a) the Bruker cantilever, and (b) the AppNano cantilever. The measured stiffnesses are within the specified ranges stated by the manufacturers (see Table III). The blue line in each figure shows the measured force by the force sensor and the red line is the fitted linear function.
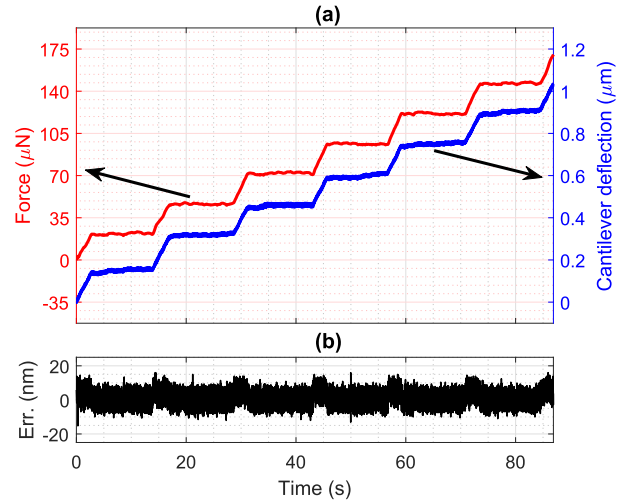
Fig. 12. (a) Closed-loop performance of the force sensor in measuring the force originated from the deflection of the Bruker cantilever, and (b) the resulted deviation of the shuttle beam's displacement from the null position. Both figures have shared the same x axis labels.

Since the internal displacement of the closed-loop force probe is zero, positioner displacement is equal to the cantilever's deflection at its tip. The actuation signal (v_a) is then converted to force from (21). In Fig. 11, the measured force is shown as a function of displacement for both cantilevers. Knowing the force and the cantilever's deflection, we can calculate the stiffnesses as 187.65 N/m, and 0.52 N/m, for the Bruker, and AppNano cantilevers, respectively. These are within the ranges specified by the manufacturers.

In another experiment, while the Bruker cantilever is in contact with the force sensor, successive ramp displacements are applied to the PI positioner, as shown in Fig. 12. The force sensor is able to precisely measure the force exerted by

TABLE IV

COMPARING THE PERFORMANCE OF THIS MEMS FORCE SENSOR WITH PREVIOUSLY REPORTED SENSORS. THE DESIGNS ARE ALSO
CATEGORIZED BASED ON WHETHER THE SENSOR FUNCTIONS IN THE OPEN LOOP (O.L.) OR THE CLOSED LOOP (C.L)

Ref.	This Work	Previous Work [20]	[4]	[6]	[17]	[18]	[19]	[33]	[34]
FSR (μN)	-211.7 to 211.5	-45.3 to 46.9	48	1	13.6	60.5	310	360	110
Res. (nN)	4.74	12.9	37.9	0.05	N/A	2.8	30	70	33.2
DNR (dB)	92.9	71.2	62.1	86.0	N/A	86.7	80.28	74.2	70.4
Design	C.L.	C.L.	C.L.	O.L.	O.L.	O.L.	C.L.	O.L.	O.L.

the cantilever. Force sensor's displacement error signal is also plotted in the figure, clearly showing that the controller is able to keep the force sensor at the null position.

VII. DISCUSSION AND COMPARISON

In this section, we compare performance of this force sensor with other designs reported in the literature. To achieve a fair comparison, the dynamic range, DNR (D_r), of the force sensor is defined as follows [20], [35], [36]:

$$D_r = 20 \log \left(\frac{FSR}{Res.} \right) \tag{25}$$

where FSR is the sensor's full-scale range. The maximum actuation voltage, that allows the force sensor to operate safely away from the snap-in instability, is experimentally obtained as $v_a = \pm 23\,V$. Considering this voltage and using (21), the FSR range of the force is calculated as $-211.7\,\mu$N to $211.5\,\mu$N. As the force sensor is operating in closed loop, the FSR range is only dependent on the actuator properties and does not change with the stiffness-adjustment voltage. Using the obtained resolution of 4.74 nN in Sec. VI-A for $V_b = 0\,V$, the dynamic range is calculated as 92.9 dB. Due to resolution enhancement at $V_b = 60\,V$ (as discussed in Sec. VI-A), the dynamic range improves to about 93.7 dB at this stiffness-adjustment voltage. Note that in calculating the dynamic range we only considered the positive side of the full-scale range. The FSR is doubled and the dynamic range is enhanced by 6 dB otherwise.

In Table IV, performance of the proposed force sensor is compared with our previous work, reported in [20], and other MEMS force sensors reported in the literature [4], [6], [17], [18], [33], [34], [37]. This force sensor has the highest dynamic range while comparatively offering a high measurement range. For example, compared to [20], our force sensor shows up to 21.7 dB increase in dynamic range. This enhancement is made possible due to the availability of a higher actuation force as well as the introduction of a displacement sensing mechanism with a sub-nanometer precision. Note that the increase in full-scale range of the open-loop force sensors reported in Table IV comes with the requirement of increasing their displacement range or stiffness. While the former adds more measurement nonlinearity, the latter decreases the device resolution. In this work, however, the use of a closed-loop configuration enables us to enhance the full scale range of the force sensor and eliminates the adverse effect of flexural nonlinearities in the measurement. The quadratic equation in (21) is used to translate the controller signal to force.

Here, as the nonlinear quadratic term of the actuation force is also captured during characterization, the full-scale range of the sensor can be defined to be equivalent to the actuation force available by the electrostatic actuators without compromising sensor's accuracy over a large range.

Similar to [20], the stiffness-adjustment mechanism implemented here enables us to adjust the sensor's stiffness based on the sample's compliance. This can prevent or reduce the possibility of damaging delicate samples, which could happen during force measurements.

VIII. CONCLUSION

In this paper, we reported the design, characterization, and control of a 1-DoF MEMS force sensor. Mechanical stiffness of the sensor can be regulated within a specific range using a parallel plate capacitive structure that is embedded in the device. The force sensor is equipped with electrostatic actuators and electrothermal displacement sensors. An on-chip leverage mechanism is incorporated to amplify shuttle beam's displacement, improving the 1σ-resolution of the electrothermal sensor to 0.645 nm.

Fundamental resonant frequency of the force sensor is located at 978 Hz. By applying 60 V to the stiffness-adjustment mechanism, this can be reduced to 568 Hz, which corresponds to 66% decrease in the device's stiffness. This capability provides an extra knob to tune the mechanical stiffness of the device based on the application at hand. The force sensor is designed to function in closed loop. Characterization of the device reveals that it can measure external forces within the range of $-211.7\,\mu$N to $211.5\,\mu$N and over a bandwidth of 44 Hz. The sensor's resolution was found to be 4.74 nN. The resolution and the full-scale range have been improved compared to our previous design, reported in [20]; resulting in a 21.7 dB increase in the dynamic range, reaching 92.9 dB. We used the force sensor to measure stiffness of two commercial cantilevers. Although the 44 Hz bandwidth of the current closed-loop system is large enough for quasi-static force measurements, it can be improved by designing a controller that offers a higher bandwidth, enabling us to measure dynamic forces with high frequency contents.

APPENDIX

In Fig. 13 schematics of the three-sectioned beam are shown. The free-body-diagram of the beam is presented in the inset. To obtain the rotational stiffness, a separate coordinate is assigned to each section of the beam, x_i ($i = 1$ to 3). Here, a known moment M is assumed to be applied to the free end
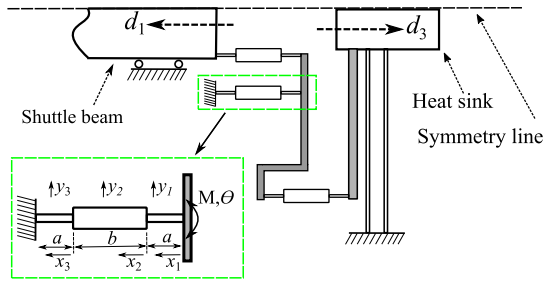
Fig. 13. The free-body-diagram of the three-sectioned beam. A known mechanical moment is applied at the end of the beam.

of the beam and the deflection angle (θ) at the same point is calculated.

Assuming Euler-Bernoulli beams, the deflection at each section of the beam can be written as:

$$y_i''(x_i) = \frac{M}{EI_i}. \tag{26}$$

where y_i'' represents the second derivatives with respect to x and I_i denotes the second moment of area of the beam's cross-section. Here, the mechanical moment M is constant along the beam. From (26), the deflection of each section is determined as:

$$y_i = \frac{M}{EI_i}\frac{x_i^2}{2} + c_{1i}x_i + c_{2i}, \quad i = 1, 2, 3. \tag{27}$$

To obtain the six unknown coefficients (i.e c_{1i} and c_{2i}), the following boundary conditions are considered:

$$\begin{cases} y_1(x_1 = a) = y_2(x_2 = 0) \\ y_1'(x_1 = a) = y_2'(x_2 = 0) \\ y_2(x_2 = b) = y_3(x_3 = 0) \\ y_2'(x_2 = b) = y_3'(x_3 = 0) \\ y_3(x_3 = a) = 0 \\ y_3'(x_3 = a) = 0 \end{cases} \tag{28}$$

Replacing (28) in (27), the unknown coefficients can be obtained. Here, the tip rotation of the beam (i.e. θ) is:

$$\theta = y_1'(x_1 = 0) = |c_{11}|. \tag{29}$$

Having the rotation at the tip of the beam, the rotational stiffness of the beam is obtained as:

$$k = \frac{M}{c_{11}} = \frac{E}{\left(\frac{a}{I_3} + \frac{b}{I_2} + \frac{a}{I_1}\right)}. \tag{30}$$

REFERENCES

[1] S. Kohyama *et al.*, "MEMS force and displacement sensor for measuring spring constant of hydrogel microparticles," in *Proc. IEEE 30th Int. Conf. Micro Electro Mech. Syst. (MEMS)*, Jan. 2017, pp. 1040–1043.

[2] A. F. Oberhauser, P. E. Marszalek, H. P. Erickson, and J. M. Fernandez, "The molecular elasticity of the extracellular matrix protein tenascin," *Nature*, vol. 393, no. 6681, pp. 181–185, May 1998.

[3] T. O. Pleshakova, N. S. Bukharina, A. I. Archakov, and Y. D. Ivanov, "Atomic force microscopy for protein detection and their physicochemical characterization," *Int. J. Mol. Sci.*, vol. 19, no. 4, p. 1142, Apr. 2018.

[4] S. I. Moore, M. B. Coskun, T. Alan, A. Neild, and S. O. R. Moheimani, "Feedback-controlled MEMS force sensor for characterization of microcantilevers," *J. Microelectromech. Syst.*, vol. 24, no. 4, pp. 1092–1101, Aug. 2015.

[5] M. B. Coskun, S. Moore, S. O. R. Moheimani, A. Neild, and T. Alan, "Zero displacement microelectromechanical force sensor using feedback control," *Appl. Phys. Lett.*, vol. 104, no. 15, Apr. 2014, Art. no. 153502.

[6] J. Rajagopalan, A. Tofangchi, and M. T. A. Saif, "Linear high-resolution BioMEMS force sensors with large measurement range," *J. Microelectromech. Syst.*, vol. 19, no. 6, pp. 1380–1389, Dec. 2010.

[7] D. P. Allison, N. P. Mortensen, C. J. Sullivan, and M. J. Doktycz, "Atomic force microscopy of biological samples," *Wiley Interdiscipl. Rev., Nanomed. Nanobiotechnol.*, vol. 2, no. 6, pp. 618–634, 2010.

[8] M. B. Coskun, H. Alemansour, A. G. Fowler, M. Maroufi, and S. O. R. Moheimani, "*Q* control of an active AFM cantilever with differential sensing configuration," *IEEE Trans. Control Syst. Technol.*, vol. 27, no. 5, pp. 2271–2278, Sep. 2019.

[9] J. H. Hoh, J. P. Cleveland, C. B. Prater, J. P. Revel, and P. K. Hansma, "Quantized adhesion detected with the atomic force microscope," *J. Amer. Chem. Soc.*, vol. 114, no. 12, pp. 4917–4918, Jun. 1992.

[10] N. P. Mortensen *et al.*, "Effects of colistin on surface ultrastructure and nanomechanics of pseudomonas aeruginosa cells," *Langmuir*, vol. 25, no. 6, pp. 3728–3733, Mar. 2009.

[11] F. Gaboriaud and Y. F. Dufrêne, "Atomic force microscopy of microbial cells: Application to nanomechanical properties, surface forces and molecular recognition forces," *Colloids Surf. B, Biointerfaces*, vol. 54, no. 1, pp. 10–19, Jan. 2007.

[12] A. E. Pelling, Y. Li, W. Shi, and J. K. Gimzewski, "Nanoscale visualization and characterization of Myxococcus xanthus cells with atomic force microscopy," *Proc. Nat. Acad. Sci. USA*, vol. 102, no. 18, pp. 6484–6489, May 2005.

[13] B. Piriyanont, A. G. Fowler, and S. O. R. Moheimani, "Force-controlled MEMS rotary microgripper," *J. Microelectromech. Syst.*, vol. 24, no. 4, pp. 1164–1172, Aug. 2015.

[14] S. Yang, Q. Xu, and Z. Nan, "Design and development of a dual-axis force sensing MEMS microgripper," *J. Mech. Robot.*, vol. 9, no. 6, pp. 061011-1–061011-9, Dec. 2017.

[15] Y. Sun, S. N. Fry, D. P. Potasek, D. J. Bell, and B. J. Nelson, "Characterizing fruit fly flight behavior using a microforce sensor with a new comb-drive configuration," *J. Microelectromech. Syst.*, vol. 14, no. 1, pp. 4–11, Feb. 2005.

[16] Y. Sun and B. J. Nelson, "MEMS capacitive force sensors for cellular and flight biomechanics," *Biomed. Mater.*, vol. 2, no. 1, pp. S16–S22, Mar. 2007.

[17] J. Cailliez, M. Boudaoud, A. Mohand-Ousaid, A. Weill-Duflos, S. Haliyo, and S. Régnier, "Modeling and experimental characterization of an active MEMS based force sensor," *J. Micro-Bio Robot.*, vol. 15, no. 1, pp. 53–64, Jun. 2019.

[18] L. Zhang and J. Dong, "Design, fabrication, and testing of a SOI-MEMS-based active microprobe for potential cellular force sensing applications," *Adv. Mech. Eng.*, vol. 4, Jan. 2012, Art. no. 785798.

[19] B. Koo and P. M. Ferreira, "An active MEMS probe for fine position and force measurements," *Precis. Eng.*, vol. 38, no. 4, pp. 738–748, Oct. 2014.

[20] M. Maroufi, H. Alemansour, M. B. Coskun, and S. O. R. Moheimani, "An adjustable-stiffness MEMS force sensor: Design, characterization, and control," *Mechatronics*, vol. 56, pp. 198–210, Dec. 2018.

[21] M. Maroufi, H. Alemansour, and S. O. R. Moheimani, "A closed-loop MEMS force sensor with adjustable stiffness," in *Proc. IEEE Conf. Control Technol. Appl. (CCTA)*, Aug. 2017, pp. 438–443.

[22] M. Maroufi, A. Bazaei, A. Mohammadi, and S. O. Reza Moheimani, "Tilted beam piezoresistive displacement sensor: Design, modeling, and characterization," *J. Microelectromech. Syst.*, vol. 24, no. 5, pp. 1594–1605, Oct. 2015.

[23] M. Maroufi and S. O. R. Moheimani, "A 2DOF SOI-MEMS nanopositioner with tilted flexure bulk piezoresistive displacement sensors," *IEEE Sensors J.*, vol. 16, no. 7, pp. 1908–1917, Apr. 2016.

[24] A. G. Fowler, A. Bazaei, and S. O. R. Moheimani, "Design and analysis of nonuniformly shaped heaters for improved MEMS-based electrothermal displacement sensing," *J. Microelectromech. Syst.*, vol. 22, no. 3, pp. 687–694, Jun. 2013.

[25] Y. Zhu, A. Bazaei, S. O. R. Moheimani, and M. R. Yuce, "A micromachined nanopositioner with on-chip electrothermal actuation and sensing," *IEEE Electron Device Lett.*, vol. 31, no. 10, pp. 1161–1163, Oct. 2010.

[26] H. Alemansour, M. Maroufi, A. Alipour, and S. O. R. Moheimani, "A feedback controlled MEMS probe scanner for on-chip AFM," *IFAC-PapersOnLine*, vol. 52, no. 15, pp. 295–300, 2019.

[27] M. Maroufi and S. O. R. Moheimani, "Characterization of piezoresistive and electrothermal sensors in MEMS devices," in *Proc. IEEE SENSORS*, Oct. 2016, pp. 1–3.

[28] C. Ru, X. Liu, and Y. Sun, *Nanopositioning Technologies: Fundamentals and Applications*. Cham, Switzerland: Springer, 2016.

[29] M. Maroufi, A. G. Fowler, A. Bazaei, and S. O. R. Moheimani, "High-stroke silicon-on-insulator MEMS nanopositioner: Control design for non-raster scan atomic force microscopy," *Rev. Scientific Instrum.*, vol. 86, no. 2, Feb. 2015, Art. no. 023705.

[30] M. Maroufi, A. G. Fowler, and S. O. R. Moheimani, "MEMS for nanopositioning: Design and applications," *J. Microelectromech. Syst.*, vol. 26, no. 3, pp. 469–500, Jun. 2017.

[31] R. Legtenberg, A. W. Groeneveld, and M. Elwenspoek, "Comb-drive actuators for large displacements," *J. Micromech. Microeng.*, vol. 6, no. 3, pp. 320–329, Sep. 1996.

[32] M. Maroufi, A. G. Fowler, and S. O. R. Moheimani, "MEMS nanopositioner for on-chip atomic force microscopy: A serial kinematic design," *J. Microelectromech. Syst.*, vol. 24, no. 6, pp. 1730–1740, Dec. 2015.

[33] F. Beyeler *et al.*, "Monolithically fabricated microgripper with integrated force sensor for manipulating microobjects and biological cells aligned in an ultrasonic field," *J. Microelectromech. Syst.*, vol. 16, no. 1, pp. 7–15, Feb. 2007.

[34] K. Kim, J. Cheng, Q. Liu, X. Y. Wu, and Y. Sun, "Investigation of mechanical properties of soft hydrogel microcapsules in relation to protein delivery using a MEMS force sensor," *J. Biomed. Mater. Res. A, Off. J. Soc. Biomater.*, vol. 92A, no. 1, pp. 103–113, Jan. 2010.

[35] A. J. Fleming, "A review of nanometer resolution position sensors: Operation and performance," *Sens. Actuators A, Phys.*, vol. 190, pp. 106–126, Feb. 2013.

[36] A. Charalambides and S. Bergbreiter, "A novel all-elastomer MEMS tactile sensor for high dynamic range shear and normal force sensing," *J. Micromech. Microeng.*, vol. 25, no. 9, Sep. 2015, Art. no. 095009.

[37] C. Zhao, G. S. Wood, J. Xie, H. Chang, S. H. Pu, and M. Kraft, "A force sensor based on three weakly coupled resonators with ultrahigh sensitivity," *Sens. Actuators A, Phys.*, vol. 232, pp. 151–162, Aug. 2015.

Mohammad Maroufi received the double B.Sc. degrees in mechanical engineering and applied physics and the master's degree in mechatronics from the Amirkabir University of Technology (Tehran Polytechnic), in 2008 and 2011, respectively, and the Ph.D. degree in electrical engineering from the University of Newcastle, Callaghan, NSW, Australia, in 2015. From 2015 to 2019, he continued his career by accepting the research associate and then research scientist post-doctoral appointments at The University of Texas at Dallas, Richardson, TX, USA. He currently holds the position of Motion Sensing Hardware Engineer in industry. His research interests include development of ultrahigh-precision mechatronic systems, design and control of MEMS nanopositioners, and microsensors design and integration.

Hamed Alemansour received the B.Sc. degree in mechanical engineering from Shiraz University in 2011, and the M.Sc. degree in mechanical engineering from the Sharif University of Technology in 2013. He is currently pursuing the Ph.D. degree in mechanical engineering with The University of Texas at Dallas, Richardson, TX, USA. His current research interests include characterization and control of MEMS-based devices, and AFM microcantilevers as well as atomic precise manufacturing with scanning tunneling microscope.

S. O. Reza Moheimani (Fellow, IEEE) currently holds the James Von Ehr Distinguished Chair in Science and Technology with the Department of Systems Engineering, The University of Texas at Dallas, with appointments in Electrical and Computer Engineering and Mechanical Engineering Departments. His current research interests include applications of control and estimation in high-precision mechatronic systems, high-speed scanning probe microscopy, and atomically precise manufacturing of solid-state quantum devices. He is a fellow of the IFAC and the Institute of Physics, U.K. He is a recipient of several awards, including the IFAC Nathaniel B. Nichols Medal and the IEEE Control Systems Technology Award. He is the Editor-in-Chief of *Mechatronics*.